

Supplementary Information

Ordered Nanoporous Cellulose-Based Membranes Fabricated via Breath Figure Method for Copper Ion Detection

*Yingfan Hu,^a Xuejiao Lin,^a Xijun Wang,^{*a} Zhouyang Xiang,^a Hui Li,^b Pengcheng Ma^{*b} and
Haisong Qi^{*a}*

^a State Key Laboratory of Pulp and Paper Engineering, South China University of Technology,
Guangzhou, 510641, China

E-mail: qihs@scut.edu.cn

^b Xinjiang Key Laboratory of Separation Material and Technology, The Xinjiang Technical
Institute of Physics and Chemistry, Chinese Academy of Sciences, Urumqi 830011, China

E-mail: mapc@ms.xjb.ac.cn

Supplementary Figures

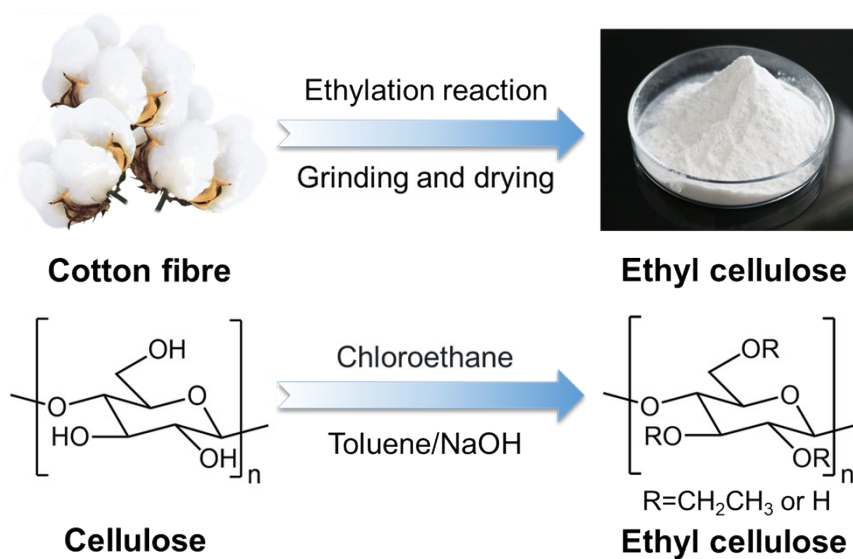


Fig. S1 The preparation process of ethyl cellulose (EC).

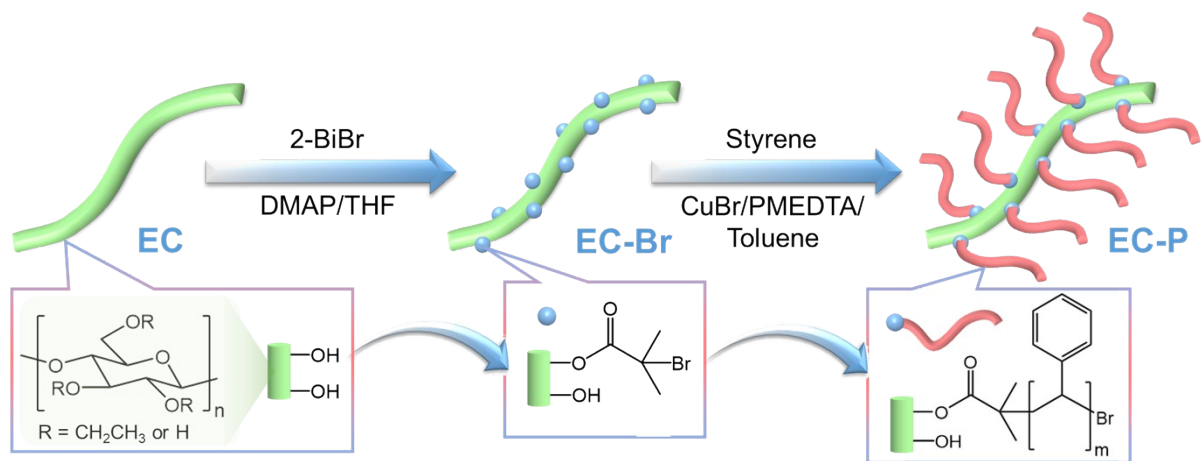


Fig. S2 The process of preparing ethyl cellulose grafted polystyrene (EC-P) by ATRP reaction.

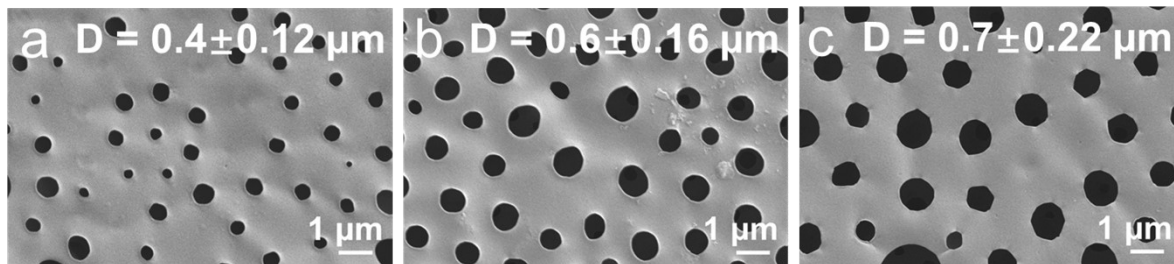


Fig. S3 SEM images of membranes prepared under different ATRP reaction conditions are shown in Fig. S3. The detailed conditions are as follows: (a) EC 10 mmol, 2-bromoisobutryl bromide (BiBB) 30 mmol, polymerization time 13 h; (b) EC 10 mmol, BiBB 30 mmol, polymerization time 7 h; (c) EC 10 mmol, BiBB 15 mmol, polymerization time 13 h.

As shown in Fig. S3, varying the ATRP reaction conditions influences both EC-P and membrane morphology. Prolonging the polymerization time increases the polymerization degree of polystyrene, resulting in smaller membrane pore sizes. During the macromolecular precursor preparation, increasing the amount of BiBB enhances the substitution degree, which also leads to smaller pore sizes. However, excessive substitution or polymerization degrees can increase the polymer solution viscosity, resulting in non-uniform pore sizes and disordered pore arrangements.^{1, 2} Based on the results in Fig. S3, condition (a) yielded smaller pores with an acceptable pore ordering degree. Therefore, the reaction condition used in Fig. S3a, with an EC to BiBB molar ratio of 1:3 and a polymerization time of 13 h, was finally selected.

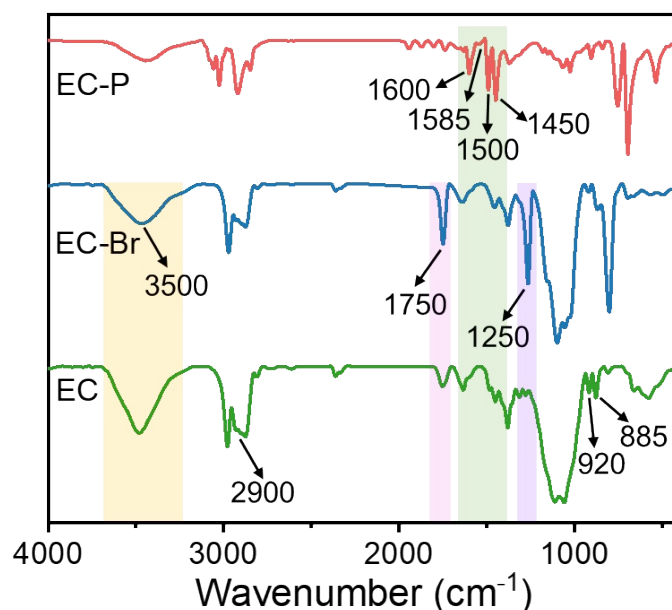


Fig. S4 Fourier transform infrared spectra of EC, EC-Br, and EC-P.

After the ethylation reaction, the peak near 2900 cm^{-1} in the FT-IR spectrum of the product belongs to methyl and methylene, and the weak absorption peaks at 920 cm^{-1} and 885 cm^{-1} belong to the characteristic absorption peaks of ethyl, indicating the successful preparation of EC. EC is a cellulose ether that does not contain ester bonds. After the synthesis of the macromolecular initiator EC-Br, the FT-IR spectrum of the product confirmed the presence of 2-bromoisobutyryloxy groups by the ester C=O stretching vibration peak at 1750 cm^{-1} and the C-O stretching vibration peak at 1250 cm^{-1} . In addition, compared with the FT-IR spectrum of EC, the stretching peak intensity of the hydroxyl group on the glucose ring of EC-Br decreased at about 3500 cm^{-1} , indicating that the hydroxyl group was partially replaced by 2-bromoisobutyl. After the completion of the second step reaction, four absorption peaks appeared in the FT-IR spectrum of the product at 1600 , 1585 , 1500 , and 1450 cm^{-1} , which are the stretching vibration peaks of the aromatic ring C=C skeleton in styrene. This indicates the successful grafting of polystyrene onto EC.²

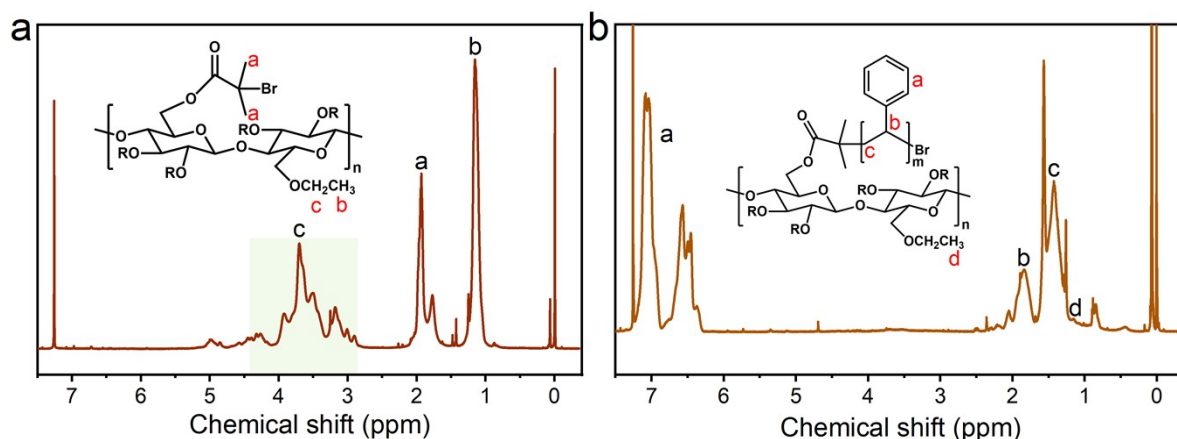


Fig. S5 ^1H NMR spectra of EC-Br (a) and EC-P (b).

For Figure S4a, the peak at 1.16 ppm is attributed to the protons of the methyl groups in EC. The series of peaks ranging from 2.9 ppm to 4.4 ppm are attributed to the chemical shifts of the protons of the methylene, methine, and hydroxyl groups in EC. The degree of ethyl substitution of EC is calculated using the following formula:

$$DS_{ethyl} = \frac{I_{1.16} \times 10}{3 \times I_{2.9-4.4} - I_{1.16}}$$

Here, DS_{ethyl} represents the degree of ethyl substitution in EC, $I_{1.16}$ denotes the integrated area of the methyl protons' chemical shift at 1.16 ppm, and $I_{2.9-4.4}$ indicates the integrated area of the protons' chemical shifts of the methylene, methine, and hydroxyl groups within the range of 2.9 to 4.4 ppm. The calculation yields DS_{ethyl} to be 2.40.

In Figure S4a, the chemical shift at 1.95 ppm is attributed to the protons of the methyl group on the bromoisobutyryl bromide moiety, and the presence of this characteristic peak indicates the successful esterification of EC. With the peak area at 1.16 ppm set to 1, the calculation is performed using the following formula:³

$$DS_{Br} = \frac{DS_{ethyl} \times 3 \times I_{1.95}}{6}$$

Here, DS_{Br} represents the degree of substitution of the bromoisobutyryl bromide group, and $I_{1.95}$ is the integrated area of the peak at the chemical shift of 1.95 ppm. The calculation yields DS_{Br} to be 0.504.

For Figure S4b, with the peak area at 1.16 ppm set to 1, the calculation is performed using the following formula:²

$$DP_{st} = \frac{DS_{ethyl} \times 3 \times I_{6.5-7.2}}{5 \times DS_{Br}}$$

Here, DP_{St} denotes the degree of polymerization of the styrene side chain, and $I_{6.5-7.2}$ refers to the integrated area of the chemical shift corresponding to the protons of the aromatic ring within the range of 6.5 to 7.2 ppm. The calculated DP_{St} is 157.

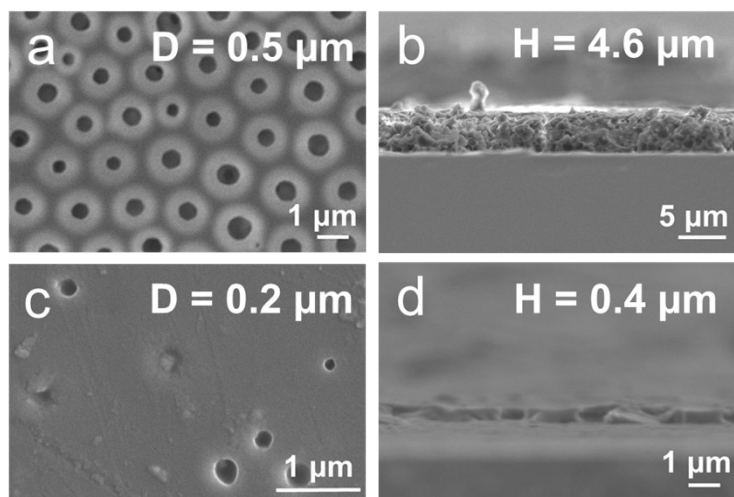


Fig. S6 (a) SEM image of the membrane surface prepared by drop casting method; (b) SEM images of membrane cross-section prepared by drop casting method; (c) SEM image of membrane surface prepared by spin coating method; (d) SEM image of membrane cross-section prepared by spin coating method (D represents the average pore diameter, H represents the membrane thickness).

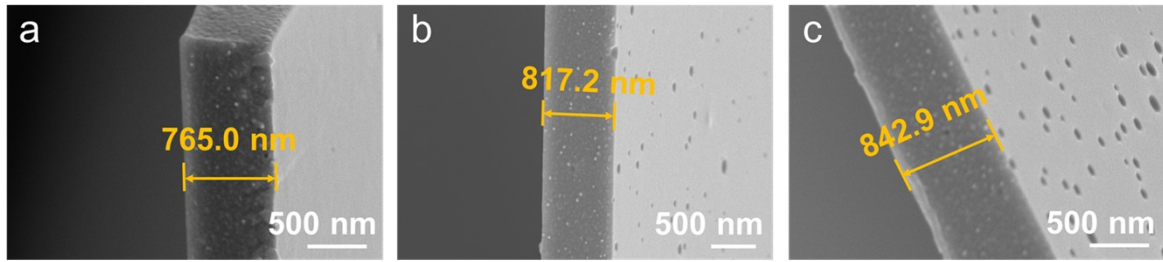


Fig. S7 Cross-sectional SEM images of membranes prepared on the water surface: (a) EC-P, (b) EC-P-S, and (c) EC-P-OH.

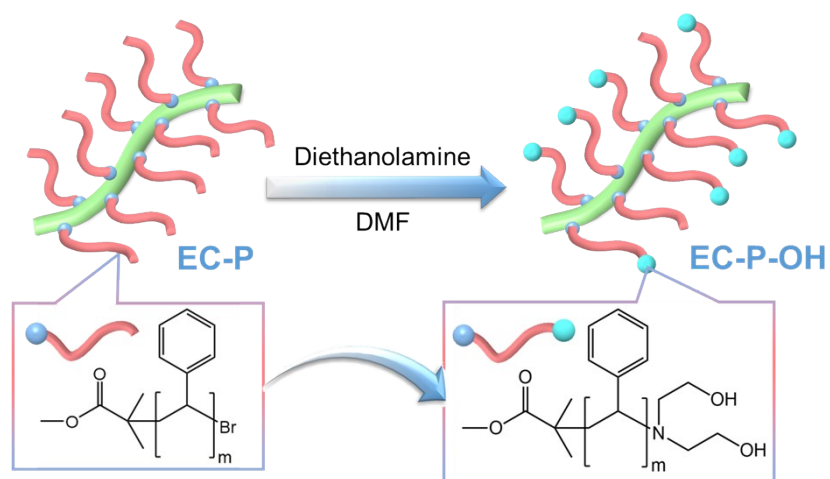


Fig. S8 EC-P-OH synthesized via nucleophilic substitution reaction between the terminal Br of polystyrene and diethanolamine.

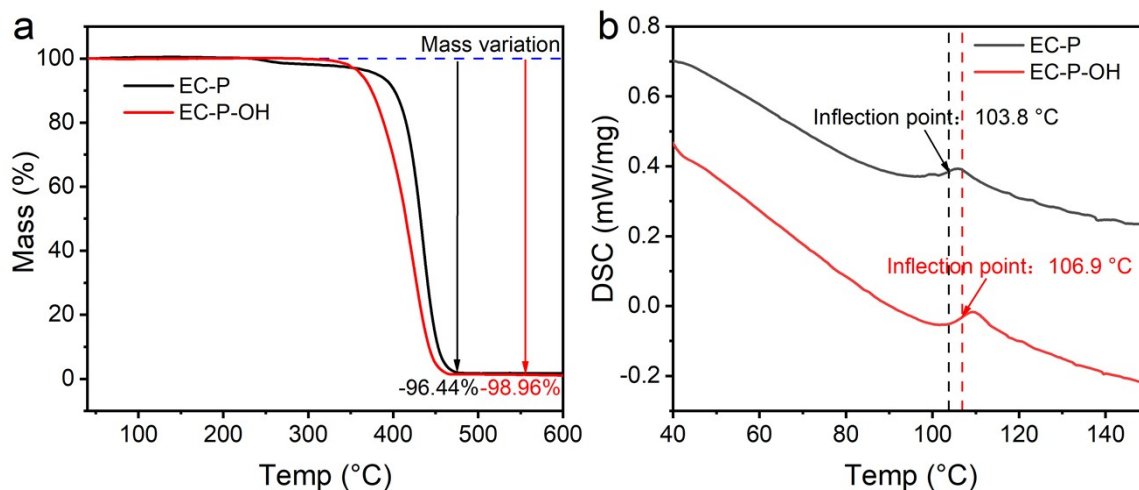


Fig. S9 TG (a) and DSC (b) analysis of EC-P and EC-P-OH.

The results show that the decomposition temperature of the product decreases, the mass change after thermal decomposition increases, and the glass transition temperature in the DSC test also increases. This is because the increased number of -OH groups makes the polymer more prone to decomposition, and during thermal decomposition, the mass proportion of -OH converting to H₂O increases, leading to a greater mass change. The increase in -OH groups also leads to more intramolecular hydrogen bonds, enhancing intermolecular interactions and restricting molecular motion, resulting in a corresponding increase in glass transition temperature. The increase in -OH groups indirectly confirms the successful synthesis of EC-P-OH.⁴

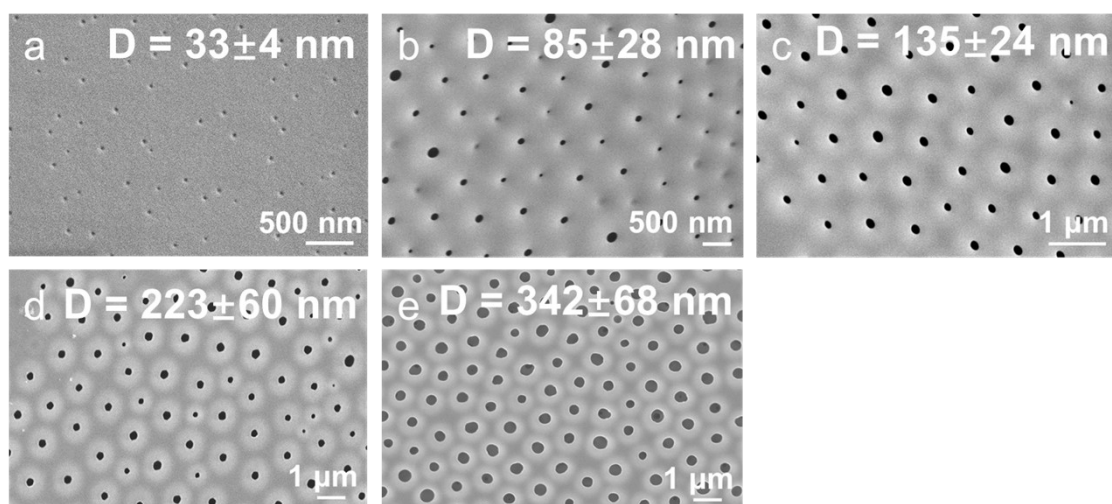


Fig. S10 Changes in pore morphology with different concentrations of Span60: (a) Span60 concentration is 0.10 mg mL⁻¹; (b) Span60 concentration is 0.15 mg mL⁻¹; (c) Span60 concentration is 0.20 mg mL⁻¹; (d) Span60 concentration is 0.25 mg mL⁻¹; (e) Span60 concentration is 0.30 mg mL⁻¹.

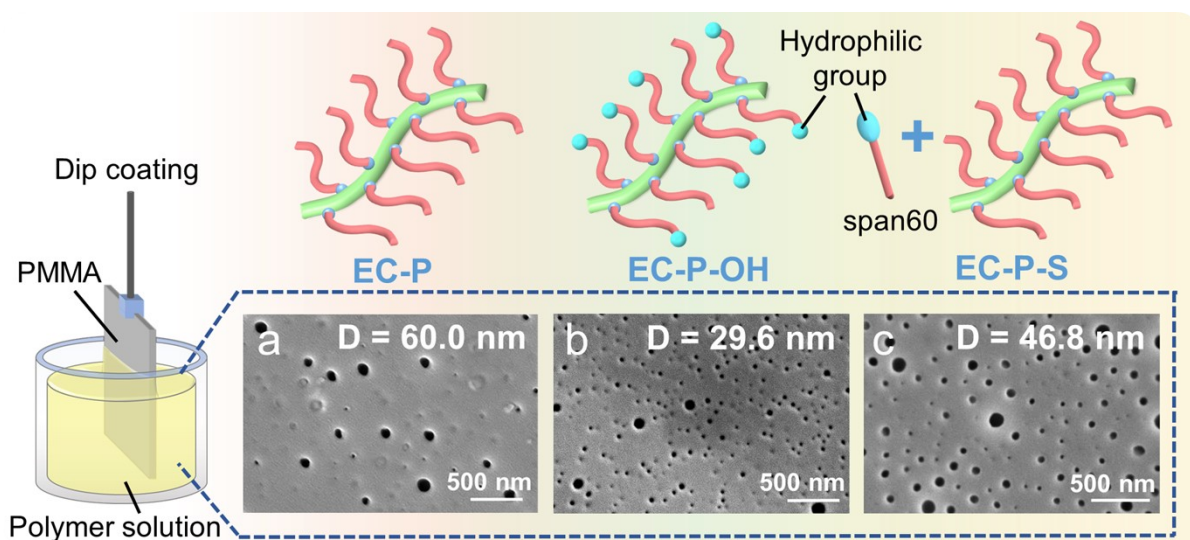


Fig. S11 SEM images of the membranes formed by dipping coat EC-P (a), EC-P-OH (b), and EC-P-S (c) solutions on PMMA substrates. The number of pores in EC-P-OH and EC-P-S membranes has significantly increased compared to EC-P membranes, which is due to the increase in hydrophilic groups.

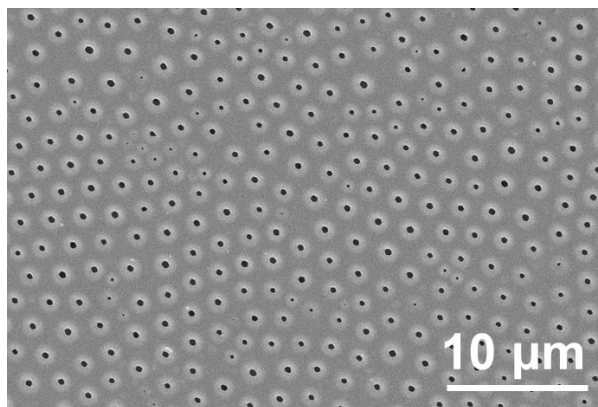


Fig. S12 EC-P-S membrane with a pore size of 346 nm as a control.

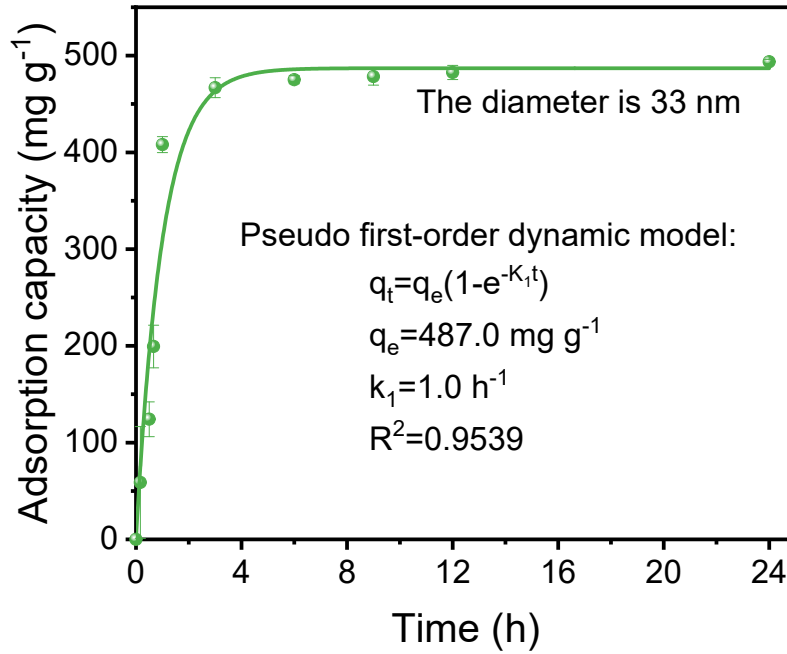


Fig. S13 The fitting curve of pseudo-first-order kinetic equation for adsorption process.

The formula for the pseudo-first-order kinetic equation of the adsorption process is:⁵

$$C = C_0 e^{-k_1 t}$$

$$q_t = q_e (1 - e^{-k_1 t})$$

In the formula, C is the equilibrium concentration of BSA (mg mL^{-1}), C_0 is the initial concentration of BSA (mg mL^{-1}), k_1 is the rate constant (h^{-1}), t is the adsorption time (h), q_t is the adsorption amount of BSA within a certain time (mg g^{-1}), and q_e is the adsorption amount of BSA at adsorption equilibrium (mg g^{-1}).

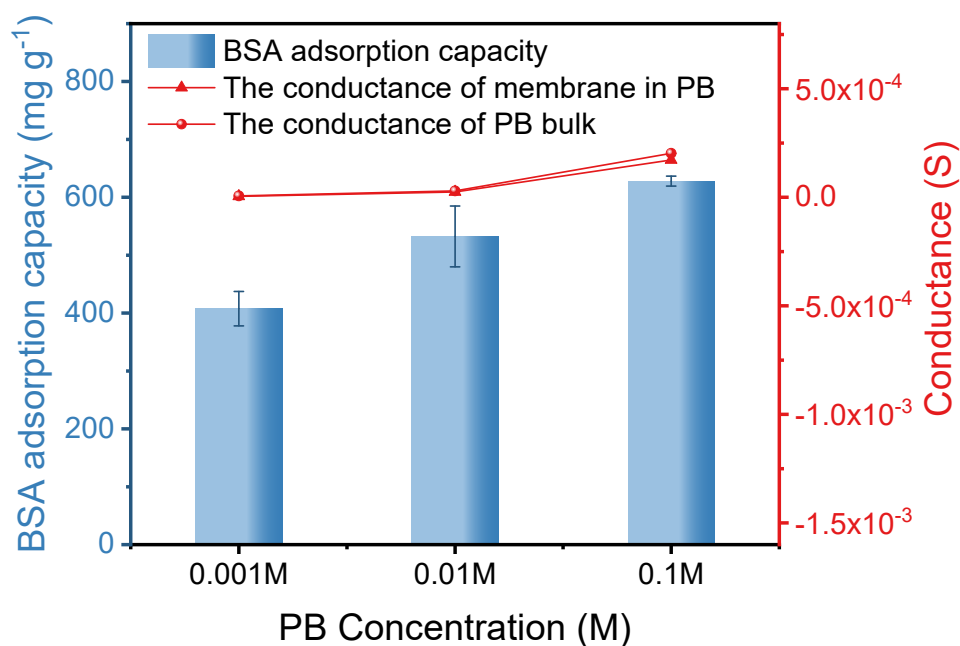


Fig. S14 The conductance of the membrane at different PB concentrations, the conductance of the bulk PB solution, and the adsorption amount of BSA in various concentrations of PB solution. The conductance of the membrane is almost the same as that of the PB solution itself, indicating that the movement of substances within the pores is similar to that in the bulk solution (EC-P-S membrane pore size is 33 nm).

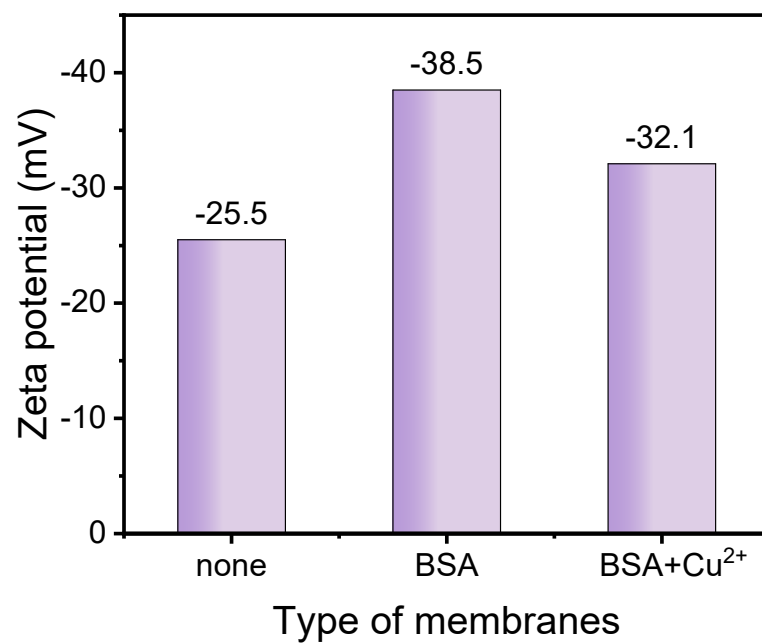


Fig. S15 Zeta potential changes of non-adsorbed membranes, BSA adsorbed membranes, and membranes in contact with Cu²⁺ after BSA adsorption (pH = 7.0).

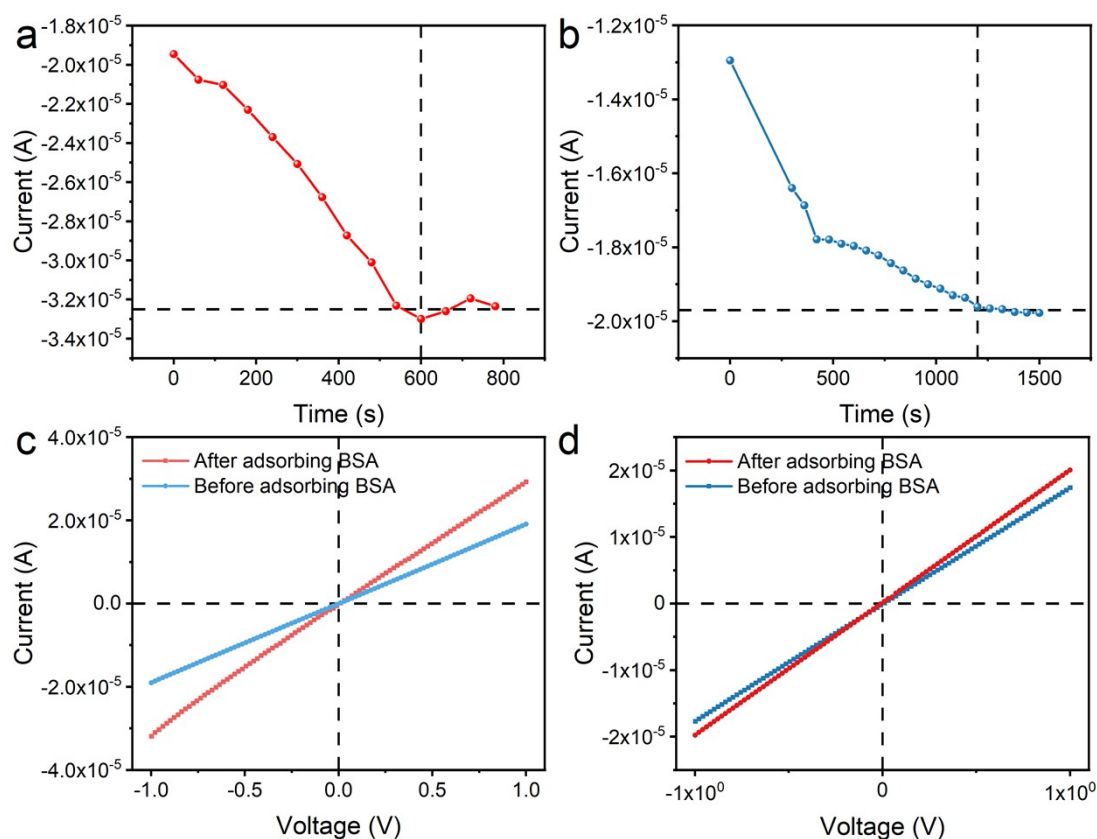


Fig. S16 (a) Change in ion current at -1.0 V over time in 0.01 M KCl solution after BSA adsorption by a membrane with a pore size of 33 nm. The ion current stabilizes after 600 seconds. (b) Change in ion current at -1.0 V over time in 0.01 M KCl solution after BSA adsorption by a membrane with a pore size of 346 nm. The ion current stabilizes after 1200 seconds. After stabilization, a comparison of the $I-V$ curves of the small-pore membrane (c) and the large-pore membrane (d) before and after BSA adsorption shows that both membranes exhibit increased ion current and conductance (slope) after BSA adsorption. This increase is attributed to the introduction of BSA, which increases the charge on the inner wall of the membrane, enhancing ion transport. This observation indirectly confirms the successful adsorption of BSA.

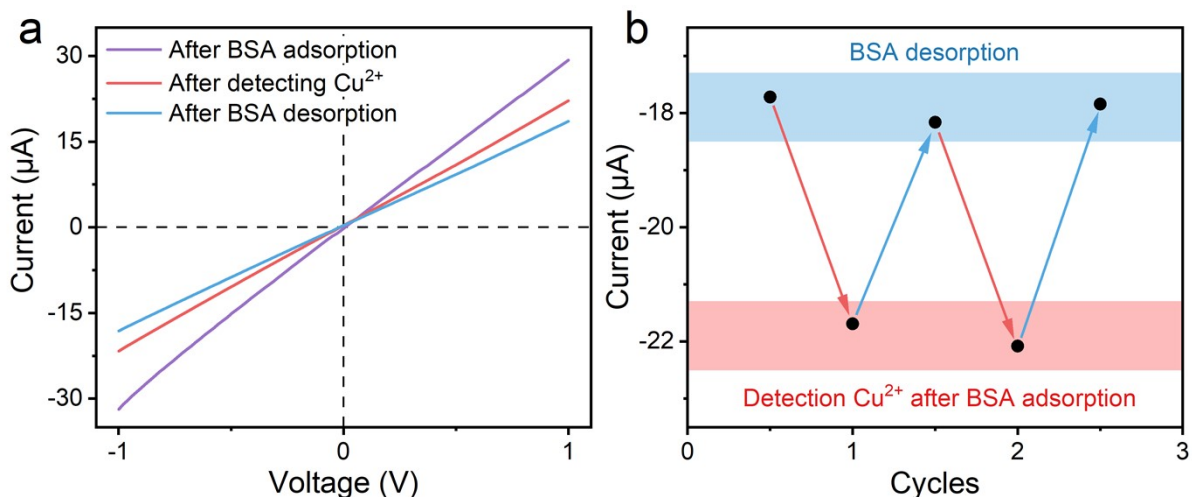


Fig. S17 Stability test for cyclic detection using EC-P-S ordered nanoporous membrane in 0.01 M KCl solution containing Cu^{2+} at concentrations of 10^{-14} M. (a) I - V curves of the EC-P-S membrane after BSA adsorption, Cu^{2+} detection, and BSA desorption processes. (b) Ion current of the EC-P-S membrane after cyclic Cu^{2+} detection and BSA desorption at a voltage of -1.0 V.

As shown in Fig. S17a, after BSA adsorption onto the EC-P-S membrane, the introduction of negative charges results in a higher ion current at -1.0 V. During Cu^{2+} detection, BSA undergoes denaturation, leading to a reduction in surface charge and a corresponding decrease in ion current. Upon desorption of BSA from the membrane, the ion current further decreases, returning to its initial state before BSA adsorption. Re-adsorbing BSA onto the membrane enables the next detection cycle.

Throughout the cycling process, the ion current after each BSA desorption remains stable at approximately -18 μA , while the ion current during Cu^{2+} detection stabilizes around -22 μA , indicating a certain level of stability in the membrane (Fig. S17b). However, after two to three cycles, the membrane tends to break due to insufficient mechanical strength, making long-term repeated use challenging. Moreover, the adsorption-desorption process requires a considerable amount of time, reducing detection efficiency. Compared to other nanoporous materials,^{6, 7} membranes fabricated using the breath-figure method offer a simpler and more cost-effective preparation process, enabling rapid large-scale production. Additionally, the modification of ion recognition units can be achieved merely through adsorption, without the need for complex chemical reactions. Therefore, using the membrane as a disposable sensor is more convenient than performing multiple adsorption-desorption cycles, significantly improving detection

efficiency. This approach is similar to disposable test strips used in colorimetric ion detection.⁸ Experimental results indicate that after multiple membrane replacements, the detection error remains minimal.

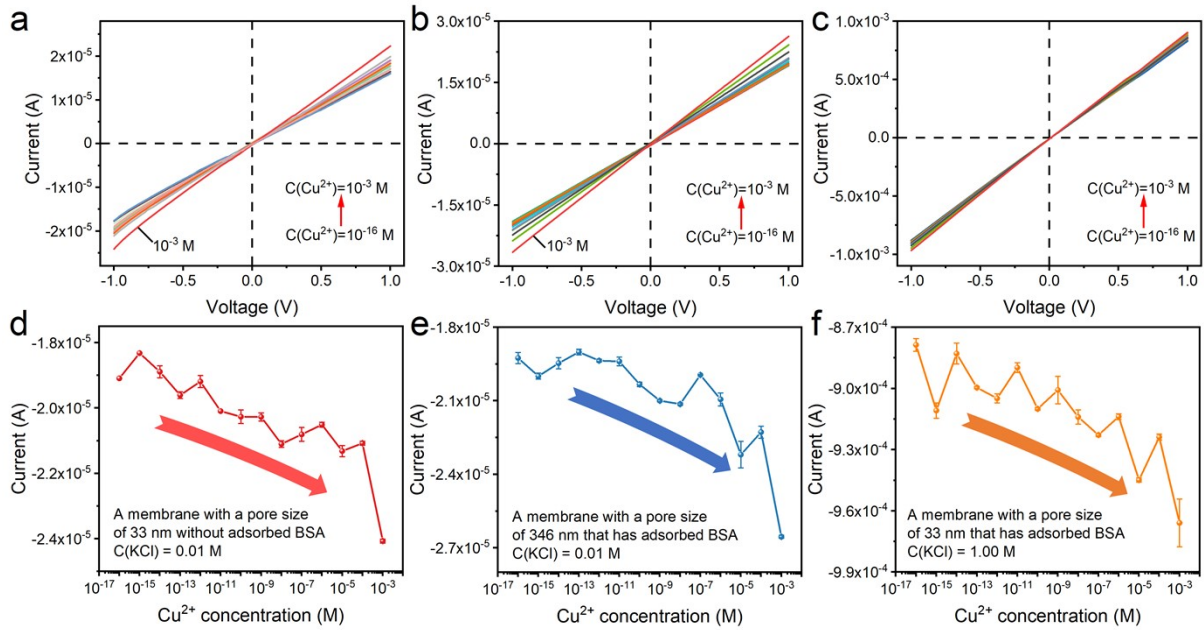
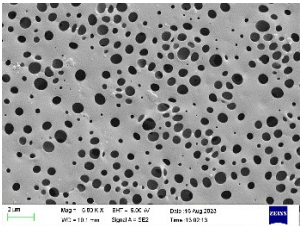
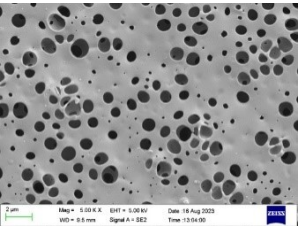
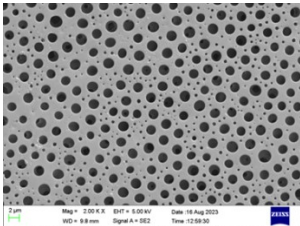
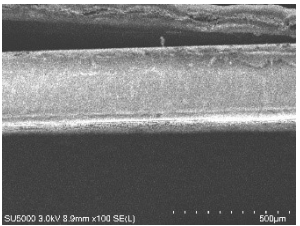
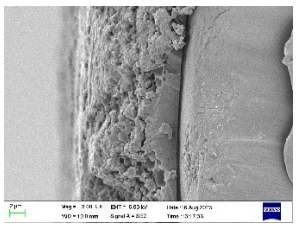
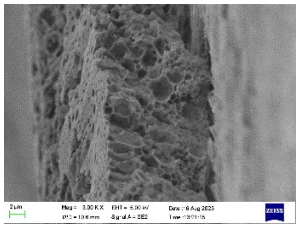
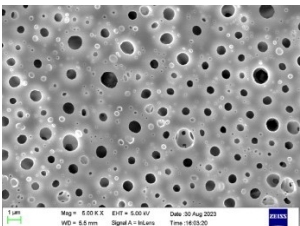
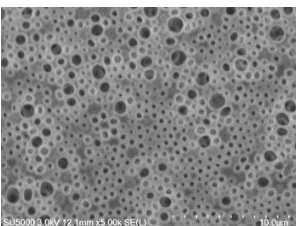
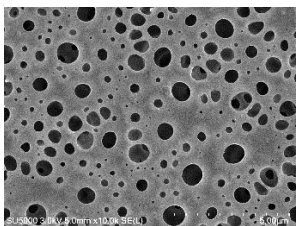


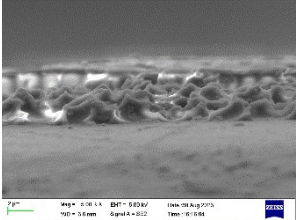
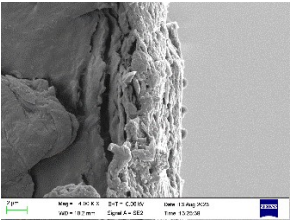
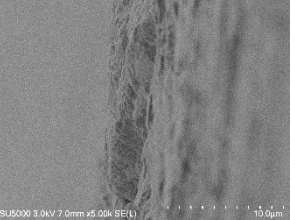
Fig. S18 (a) $I-V$ curves of small pore (33 nm) membrane without BSA adsorption at different Cu^{2+} concentrations when KCl concentration is 0.01 M. (b) $I-V$ curves of large pore (346 nm) membrane with BSA adsorption at different Cu^{2+} concentrations when KCl concentration is 0.01 M. (c) $I-V$ curves of small pore membrane (33 nm) with BSA adsorption at different Cu^{2+} concentrations when KCl concentration is 1.00 M. (d), (e), and (f) is the relationship between the ion current at -1.0 V and the concentration of Cu^{2+} in the above three cases. Although there is some fluctuation in ion current with the change of Cu^{2+} concentration, overall, the absolute value of the current shows an increasing trend.

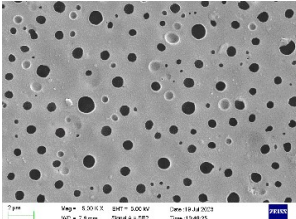
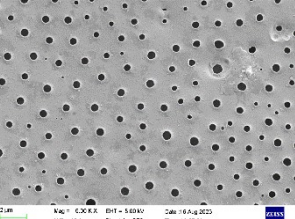
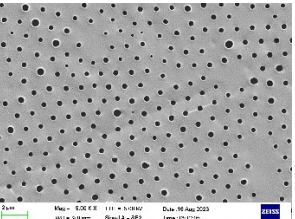
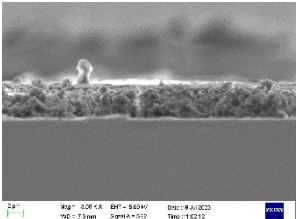
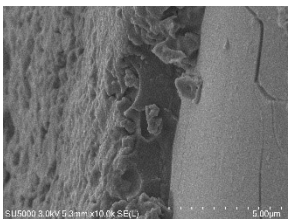
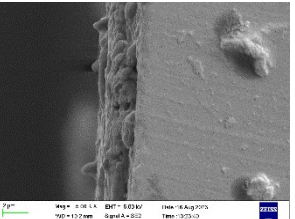
Supplementary Tables

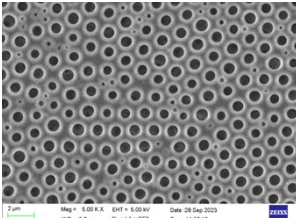
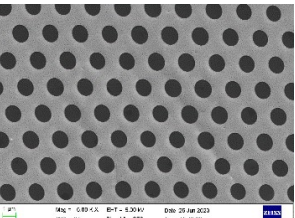
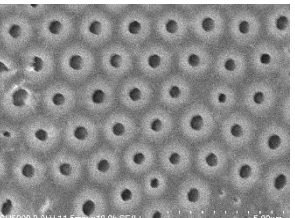
Table S1 Surface SEM and cross-sectional SEM images of membranes prepared on different substrates for which the average pore diameter (D), the coefficient of variation of the pore (CV), the conformational entropy (S), and the thickness of the membrane (H) were calculated.

Substrate	PE	PP	PTFE
Surface SEM image			
D (μm)	0.483	0.546	0.832
CV	60.52%	61.20%	81.10%
S	1.10	1.13	1.12
Cross-section SEM image			
H (μm)	5.037	10.925	13.445

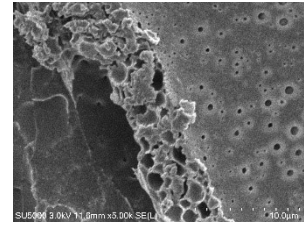
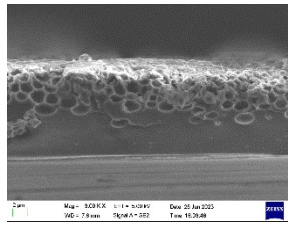
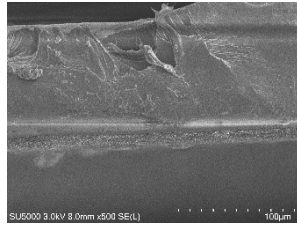
Substrate	Pa66	ABS	PMMA
Surface SEM image			
D (μm)	0.294	0.374	0.285
CV	91.18%	59.97%	40.00%
S	1.22	1.14	1.19

Cross-section SEM image			
H (μm)	3.108	3.139	2.452

Substrate	Glass	Mica	Silicon wafer
Surface SEM image			
D (μm)	0.515	0.428	0.335
CV	47.11%	27.08%	13.33%
S	1.18	1.04	0.93
Cross-section SEM image			
H (μm)	4.243	2.951	2.380

Substrate	PET	PVC	PC
Surface SEM image			
D (μm)	0.614	1.224	0.457
CV	33.39%	10.88%	19.51%
S	1.04	0.85	1.05

Cross-
section
SEM image



H (µm)

10.436

11.066

4.061

Table S2 Calculation of Du values for different pore sizes at different KCl concentrations (Zeta potential is -25.5 mV).

KCl					
concentration (M)	λ_D (nm)	σ	ρ	h (nm)	Du
1	0.30	-5.90×10^{-2}	-9.63×10^7	33	0.0185
10^{-1}	0.96	-1.85×10^{-2}	-9.63×10^6	33	0.0570
10^{-2}	3.04	-5.83×10^{-3}	-9.63×10^5	33	0.1827
10^{-3}	9.61	-1.84×10^{-3}	-9.63×10^4	33	0.5781
10^{-4}	30.40	-5.82×10^{-4}	-9.63×10^3	33	1.8245
10^{-5}	96.13	-1.84×10^{-4}	-9.63×10^2	33	5.7587

KCl					
concentration (M)	λ_D (nm)	σ	ρ	h (nm)	Du
1	0.30	-5.90×10^{-2}	-9.63×10^7	346	0.0018
10^{-1}	0.96	-1.85×10^{-2}	-9.63×10^6	346	0.0055
10^{-2}	3.04	-5.83×10^{-3}	-9.63×10^5	346	0.0175
10^{-3}	9.61	-1.84×10^{-3}	-9.63×10^4	346	0.0553
10^{-4}	30.40	-5.82×10^{-4}	-9.63×10^3	346	0.1746
10^{-5}	96.13	-1.84×10^{-4}	-9.63×10^2	346	0.5512

The calculation process is as follows:

The total conductivity of the nanochannels κ can be represented as a sum of contributions from the bulk conductivity κ_{bulk} (Sm) and the surface conductivity κ_s (Sm²), described by the following formula:⁹

$$\kappa = \kappa_{bulk} + \frac{\kappa_s}{h}$$

Here, h is the height of the channel (diameter). The Dukhin number (Du) is introduced to quantify the contribution of surface charge to total conductivity. It is defined as the ratio of

surface conductivity (κ_s) to bulk conductivity (κ_{bulk}), divided by the diameter (h). This dimensionless number helps in understanding the relative importance of surface conduction compared to bulk conduction in a given system. Mathematically, the Dukhin number can be approximated as:⁹

$$Du = \frac{\frac{\kappa_s}{h}}{\frac{\sigma}{\rho}} \approx \frac{\sigma}{\rho h}$$

where σ is surface charge density (C m⁻²), ρ is the bulk ion charge density (C m⁻³). σ is calculated by the following formula:¹⁰

$$\sigma = \frac{\varepsilon \varepsilon_0 \tau}{\lambda_D}$$

where ε is the relative dielectric constant, ε_0 is the vacuum dielectric constant (8.85419×10^{-12} C m⁻¹ V⁻¹), τ is the zeta potential (mV), λ_D is the Debye length (nm), which is the thickness of the double layer. At 25 °C, for a 1:1 electrolyte solution with a concentration of c_i , the thickness of the electric double layer is expressed as:¹¹

$$\lambda_D = \frac{\sqrt{\varepsilon_0 \varepsilon_r R T}}{\sqrt{2000 F^2 I_s}} = \frac{3.04 \times 10^{-10}}{\sqrt{I_s}}$$

Here, ε_r is the dielectric coefficient of water at 25 °C (78.36), R is the gas constant, T is the temperature (K), F is the Faraday constant, I_s is the ion strength, and its expression is:

$$I_s = \frac{1}{2} \sum c_i z_i^2$$

Where c_i is the molar concentration (mol L⁻¹) of ion i , and z_i is the valence charge of ion i . For a KCl solution, the calculated value of I_s is the same as the concentration of KCl. Thus, the λ_D values for KCl solutions of different concentrations can be calculated accordingly.

Calculate ρ using the following formula:⁹

$$\rho = 10^3 C N_A e$$

Here, C is the bulk ion concentration, N_A is the Avogadro number, and e is the electron charge.

Table S3 Summary of literature on electrochemical detection of Cu²⁺. (RPS is Resistive Pulse Sensing, and ICR is Ionic Current Rectification, AAO is anodic aluminum oxide)

Type of Nanopore	Limit of Detection	Linear Range	Sensing Principle	References
α -hemolysin	4×10^{-8} M	-	RPS	12
α -hemolysin	6.7×10^{-11} M	-	RPS	13
α -hemolysin	1.2×10^{-8} M	8×10^{-8} - 2×10^{-5} M	RPS	14
α -hemolysin	1.6×10^{-8} M	3×10^{-8} - 1×10^{-6} M	RPS	15
Glass nanopipette	-	4×10^{-6} - 1×10^{-4} M	ICR	16
Glass nanopipette	1.05×10^{-6} M	7.5×10^{-6} - 6×10^{-5} M	ICR	17
Glass nanopipette	-	1×10^{-6} - 4×10^{-5} M	ICR	18
PET nanochannel	-	1×10^{-5} - 5×10^{-4} M	ICR	19
PET nanochannel	-	1×10^{-14} - 1×10^{-7} M	ICR	20
PET nanochannel	1×10^{-15} M	1×10^{-15} - 1×10^{-3} M	ICR	7
Nanochannel array of AAO	1×10^{-16} M	3.37×10^{-16} - 2.37×10^{-2} M	ICR	21
This work	1×10^{-16} M	1×10^{-16} - 1×10^{-3} M	Ionic current	-

References

1. W. Liu, R. Liu, Y. Li, W. Wang, L. Ma, M. Wu and Y. Huang, *Polymer*, 2009, **50**, 2716-2726.
2. D. Shen, H. Yu and Y. Huang, *Cellulose*, 2006, **13**, 235-244.
3. Y. B. Jiang, Y. Y. Zhang, B. L. Chen and X. Y. Zhu, *J. Membr. Sci.*, 2019, **588**, 117222.
4. L. W. Zhu, Y. Ou, L. S. Wan and Z. K. Xu, *J Phys Chem B*, 2014, **118**, 845-854.
5. J. C. Ma, X. Q. Wang, Q. X. Fu, Y. Si, J. Y. Yu and B. Ding, *ACS Appl. Mater. Interfaces*, 2015, **7**, 15658-15666.
6. T. Ma, S. Tan, R. Yuan, X. Kang, P. Guo, Y. Tong, T. Zhao, Z. Xiao, Z. Cao, L. Li and S. Balme, *Chem. Eng. J.*, 2023, **475**.
7. P. An, Z. Zhang, J. Yang, T. Wang, Z. Wang, C.-L. Sun, C. Qin and J. Li, *Anal. Chem.*, 2023, **95**, 13456-13462.
8. H. Zhang, C. Xia, G. Feng and J. Fang, *Sensors*, 2021, **21**, 5998.
9. M. Garg and I. Zozoulenko, *ACS Appl Bio Mater*, 2021, **4**, 8301-8308.
10. H.-J. Butt, K. Graf and M. Kappl, *Physics and chemistry of interfaces*, John Wiley & Sons, 2023.
11. P. Luan, Y. Zhao, Q. Li, D. Cao, Y. Wang, X. Sun, C. Liu and H. Zhu, *Small*, 2021, **18**, 2104320.
12. G. H. Wang, L. Wang, Y. J. Han, S. Zhou and X. Y. Guan, *Biosensors & Bioelectronics*, 2014, **53**, 453-458.
13. L. P. Liu, Z. Fang, X. J. Zheng and D. M. Xi, *ACS Sens.*, 2019, **4**, 1323-1328.
14. Y. L. Guo, F. F. Jian and X. F. Kang, *RSC Adv.*, 2017, **7**, 15315-15320.
15. K. Pyrzynska, K. Kilian and M. Pegier, *Molecules*, 2022, **27**, 3311.
16. P. Actis, B. Viložny, R. A. Seger, X. Li, O. Jejelowo, M. Rinaudo and N. Pourmand, *Langmuir*, 2011, **27**, 6528-6533.
17. L. Z. Chen, H. L. He, X. L. Xu and Y. D. Jin, *Anal. Chim. Acta*, 2015, **889**, 98-105.
18. P. Hu, Y. Wang, Y. Zhang and Y. D. Jin, *Anal. Chem.*, 2022, **94**, 14273-14279.
19. J. P. Hsu, Y. C. Chen and C. T. Wu, *J. Taiwan Inst. Chem. Eng.*, 2020, **109**, 145-152.
20. L. K. Müller, I. Duznovic, D. Tietze, W. Weber, M. Ali, V. Stein, W. Ensinger and A. A. Tietze, *Chemistry-a European Journal*, 2020, **26**, 8511-8517.
21. X. P. Zhao, S. S. Wang, M. R. Younis, X. H. Xia and C. Wang, *Anal. Chem.*, 2018, **90**, 896-902.